Molecular Dynamics Simulation of the Electrochemical Cell Design for All-vanadium Redox Flow Battery

Anant Babu Marahatta [a,b*]

[a] *Department of Chemistry, Amrit Science Campus, Tribhuvan University, Kathmandu, Nepal.*
[b] *Engineering Chemistry and Applied Science Research Unit, Kathford International College of Engineering and Management (Affiliated to Tribhuvan University), Kathford International Education and Research Foundation, Lalitpur, Nepal.*

Author's contribution

The sole author designed, analyzed, interpreted and prepared the manuscript.

Original Research Article

ABSTRACT

Being the most potential battery candidate for the electrical grids connections due to having promising electrochemical energy storing abilities, vanadium redox flow battery (VRFB) is widely recognized state-of-the-art technology in renewable energy sectors. Despite its uniqueness of utilizing "all-vanadium" redox couples as the most prospective electrolyte materials, and their conspicuous technological functionalizations, the research works concentrated into its internal operational mechanisms of the cell at both ideal & different state-of-charges are still in the primitive stage. This MD simulation based theoretical insights aiming at revealing benchmark quantitative information on the interfacial micro structures around its Nafion$-$117 type proton exchange membrane, the intense hydration affinities of its adjacent state bare V^{n+} ions, and the closed proximity around the H_2O, H_3O^+, & Nafion-SO_3^-, etc. at nanometer scale would be a stepping-stone to its technological advancement. The general results presented here illuminate that the VRFB-electrolyte hosting H_2O molecules and protons in Hydronium (H_3O^+), Eigen ($H_5O_2^+$), & Zundel

Corresponding author: E-mail: abmarahatta@gmail.com, anant.marahatta@kathford.edu.np;

($H_9O_3^+$) states are distributed in a pattern identical to that in a purely bulk water system, and are dynamically used up for exhibiting facile proton conduction. Besides this, the significant departures of the SO_3^- units of the Nafion−117 at water content (λ) = 22 predicted herein confirms its experimentally observed feature of easy accommodating H_2O, H_3O^+, & V^{n+} in between them; elucidating the reasons behind its atypical proton conductivity & ionic mobility rates under wet conditions. The MD trajectories based radial distribution function (RDF) predicted $V^{n+}-$ OH_2 radial distances validate the extreme hydration affinities of the bare adjacent V^{n+} ions plus their stabilizing propensities with free H_2O molecules as established earlier by the DFT based quantum mechanical method.

1. INTRODUCTION

The unique recognition of the d-block metal atoms (M) present in the periodic table is because of their transitional behavior and many other notable characteristic features [1]. Among them, the variable oxidation states (hereafter, OSs) M^{n+}: every valence states remain unstable both in the solution and crystalline states due to having irregular electronic configuration ($ns^{1-2}nd^{1-10}$), high and intense charge density, relatively smaller yet irregularly varied ionic radii, stronger complex forming tendencies with different types of ligands $[ML_m]^{n+}$, immediate & subsequent hydration abilities, and significant variation on the acidity of M^{n+} in $[ML_m]^{n+}$ are the most prevalent traits. More specifically, the variable M^{n+} OSs are conceded in hydration chemistry due to their remarkable preferences of undergoing immediate thermodynamic stabilizations *via* the closed association with distinct number of H_2O molecules ($H_2O \rightarrow M^{n+}$); owing to the formation of specific type coordinated complexes $[M(H_2O)_m]^{n+}$ [1,2]. Among the $3d$−series elements, the most stable metallic form is vanadium (atomic number Z = 23). It exhibits many distinctive attributes including recognizably different yet surprisingly stable adjacent V^{n+} OSs; n = +2, +3, +4, and +5 with unique & contrasting colors of their aquo complexes (lilac, green, blue, and yellow respectively), incredibly smaller ionic radii & intense charge density, dissimilar thermodynamic stabilities & magnetic/superconducting properties, medium−hard, ductile, malleable, and brittleness metallic properties, excellent catalytic & corrosion resisting abilities, good alloy forming propensities with many precious metals, etc. [2-5] because of which it has been using extensively as: (a) an electrolyte material for the stable and long lasting batteries, (b) a potential industrial catalyst, (c) a major chemical constituent for manufacturing steel alloys, tough corrosion resisting & high strength engineering materials, superconducting alloys, electromagnets, nanotubes, good electrically conducting but thermally insulating tools, etc.

Actually, in the aqueous type media, the adjacent bare V^{n+} OSs most preferentially undergo hydration reactions by forming the variably configured hydrated complexes $[V(H_2O)_m]^{n+}$ having distinctive electronic stability and coordination chemistry [2,3]. In the real world, these hydrated forms are very frequently confronted in: (a) contact process of manufacturing H_2SO_4; (b) vanadium redox flow (hereafter, VRFB) and vanadium solid−salt battery (hereafter, VSSB) technologies ("all vanadium" redox couples (V^{3+}/V^{2+} and V^{5+}/V^{4+}) are used as their electrolyte materials); (c) mineralogical and geological surveys; (d) humid hydrosphere and atmospheres; (e) biological and oceanic life systems; (f) marine invertebrates' blood cells ($V^{n+}-$ hydrated states serve as a defense mechanism) [4-9], etc. In particular, the hydration preferences of the V^{n+} ions present in the VRFB -electrolytes play very critical roles as they are known for causing "water-flooding" in its proton exchange membrane (hereafter, PEM) [10]. Since the VRFB cell utilizes moderately concentrated H_2SO_4 (*aq.*) based $V^{n+}-$ anolyte and catholyte matrices separated through the Nafion type PEM, the expected suspended particles in them are V^{n+}, H_2O, H_3O^+, and HSO_4^- ($[SO_4^{2-}]$ is negligible as 1M H_2SO_4 (*aq.*) maintains $[HSO_4^-]:[SO_4^{2-}]$ ratio 99:1 [11]). Despite the most possible existence of the VRFB−electrolyte V^{n+} adjacent OSs in $[V(H_2O)_6]^{2+}$, $[V(H_2O)_6]^{3+}$, $[VO(H_2O)_5]^{2+}$, and $[VO_2(H_2O)_3]^+$. H_2O forms [12-17], present study has incorporated bare V^{n+} adjacent OSs into the VRFB - molecular dynamics (hereafter, VRFB−MD) simulator with the aim of quantifying their hydration preferences in the aqueous media. Amid the various experimental and *ab initio* theoretical research

works concentrated into the complexing affinities of the bare V^{n+} ions with oxygen-donor solvents [12-17], the MD based quantitative studies centralizing fully into the VRFB–issues at different state of charges (hereafter, SOCs) such as hydration preferences of the bare V^{n+} adjacent OSs (causing water–flooding), inter–particle interactions (affecting protonic & ionic mobility rates), PEM's interphasial microstructures & the immediate environment around its proton conducting sites SO_3^- (influencing proton transport rates), etc. are still in the preliminary stage. Beside this, the MD based theoretical/computational perspectives of the battery are highly demanding in the field of functionalizing/ developing its advanced materials as well as in advancing/designing wide range Battery systems. In this sense, this integrative report of the VRFB–MD simulation derived results stands as a doctrine article.

Since MD is simply a computer simulation in which atoms and molecules are allowed to interact for a definite period of time t through the integrative package of the Newton's equations of motion, it acts as an indispensable theoretical mean of converting presumed microscopic properties of the N–body particle systems into the measurable macroscopic observables *via* the tools of statistical mechanics [18]. Actually, in MD simulation, every molecules are described on the basis of simple harmonic oscillator approximations, the time evolution of their intramolecular (bond lengths E_{bond}, bond angles E_{angle} , and torsional angles $E_{torsion}$) and intermolecular (non-bonding van der Waals E_{vdW} and electrostatic E_Q) interactions (interactions potential; $U = E_{bond} + E_{angle} + E_{torsion} + E_{vdW} + E_Q$) must be estimated by employing the concerned force fields packages hosting a complete set of the mathematical equations, and the closely associated geometrical constants [19,20]. Among the diverse force field packages (MM2/MMP2, AMBER, CHARMM, DREIDING, AMOEBA, etc. [21]), the DREIDING; a generic force field, is computationally employed in the current VRFB–MD simulator for the hybridization based force constants, and the related equilibrium geometrical parameters [19-21]. A relatively more novel AMOEBA force field is also practically realized for the sake of addressing non-bonding type V^{n+} ionic interactions with the substantial short–range charge penetration, many-body charge transfer & polarization effects [22,23]. Besides these, the polarizable atomic multipole scheme [24], and the five-interacting-sites model with switching function [25] are accessed in order to address the issues related to the intermolecular type interactions between the H_2O molecules themselves and with the H_3O^+ ions respectively. And, the velocity verlet propagation scheme is executed while assessing all the required equations of motion of the particles and their integrative mathematical forms [26-28]. Thus programmatically designed VRFB–MD simulator with the specific numbers of the concerned electrolyte constituent particles such as V^{n+}, H_2O, H_3O^+, HSO_4^-, and Nafion fragments (Table 1) can simulate the latter dynamically, and enables us to determine their positions $r(t)$ & velocities $v(t)$ at time t in the presence of predefined initial positions $r_i(t_0)$ & velocities $v_i(t_0)$. In the course of retrieving all the needful macroscopic observables from the MD derived trajectories, the esteemed analytical mathematical tool called Radial Distribution Function (RDF) $g(r)$ is used. On the same basis, the micro-structures of the molecular assembly around the territory of any reference particle which in fact confers the optimum probability of finding free H_2O molecules at a specific distance d from the bare V^{n+} ions, H_3O^+, Nafion, and vice versa are predicted quantitatively. These quantitative analyses eventually provide the benchmark information required to verify why the bare V^{n+} adjacent OSs show high preferences towards complexing with the distinct number of free H_2O molecules by forming uniquely stable yet dissimilarly coordinated aqua complexes. In terms of these microanalyses, the RDF $g(r)$ not only tops the experimental ways of depicting molecular arrangement around the any specific reference particle but also acts as a precise mathematical mean of quantifying many experimentally immeasurable macroscopic properties. The structure of this paper is organized as: Theoretical Approaches and Computational Details are outlined in section 2, Results and Discussions are presented in section 3, and Conclusions are summarized in section 4.

2. COMPUTATIONAL DETAILS

As per the internal working mechanism of the VRFB cell at different SOCs, the V(II)/V(III) and V(IV)/V(V) states diffuse into the PEM from the negative and positive half cells respectively along with the additional ionic/molecular species such as H_2O, H_3O^+, and HSO_4^- present predominantly in both catholyte and anolyte solutions. Actually, the 1M H_2SO_4 (*aq.*) based solution of the vanadyl sulfate $VOSO_4 \cdot XH_2O$ is used as a precursor of the VRFB working "all-vanadium" electrolytes,

the prevalent Sulphur centered ionic species maintained in it through the two-steps H_2SO_4 dissociation are HSO_4^- (the quantitative amount of $[SO_4^{2-}]$ is negligible as $[HSO_4^-]:[SO_4^{2-}]$ is $99:1$ whenever $[H_2SO_4] \geq 1M$ [11]). Again, the VRFB using Nafion−117 membrane; an insoluble but swelling type PEM in the polar solvent, with polar (P) and non-polar (N) groups shows relatively better proton conductivity whenever the equivalent weight $EW \geq 1100$ ($EW = 100x + 446$; where x signifies number of non-polar groups which is generally $6 < x < 7$), and the water content $\lambda = 22$ ($\lambda = \frac{\text{Number of } H_2O}{\text{Number of } SO_3^{2-}}$) in the liquid water system [28]. Therefore, the current VRFB simulation systems were designed under the conditions: (a) Set-1: V(II) ions; (b) Set-2: V(III) ions; (c) Set-3: V(IV) ions; and (d) Set-4: V(V) ions explicitly with the required number of the additional H_2O, H_3O^+, and HSO_4^- particles listed in Table 1 so that the net λ value of the Nafion−117 becomes not less than 22. The close−up graphical view of each simulation set is displayed in Fig. 1 where the adjacent vanadium ions V^{2+}, V^{3+}, VO^{2+} (V^{+4}), and VO_2^+ (V^{5+}) are seen in the bare states.

The entire MD simulation script was designed and run iteratively as shown in the Scheme 1. The specific controlling parameters such as time−step, length of the trajectory, intermittent geometry/energy sampling intervals, annealing conditions, etc. are explicitly mentioned. The DREIDING force field was implemented computationally for hybridization (atomic radii related bonding parameters) based force or spring constants for bonding potential (K_{IJ}), and equilibrium geometrical parameters such as bond lengths R_{IJ}° (*Eq.*1), bond angles $\cos\theta_{IJK}^\circ$ (*Eq.*2), and torsional parameters (*Eq.*3) for each molecular/ionic species, and for the intermolecular Van der Waals (*Eq.* 4) and coulombic type (*Eq.* 5) nonbonding interactions. The AMOEBA force field was incorporated into the MD simulator for addressing the non-bonding V^{n+} ions interactions with substantial short-range charge penetration, many-body charge transfer & polarization effects by utilizing the *ab initio* derived multiple moments values, and inserting explicitly the permanent dipoles & quadrupoles in interaction potential term U (*Eq.* 6) [22,23]:

Table 1. Number of particles present in each simulation set

Vanadium oxidation states	No. of bare V^{n+} ions	No. of Nafion chain $(N_7P)_{10}$	No. of SO_3^-	No. of H_3O^+	No. of HSO_4^-	No. of H_2O	Water content (λ)
V(II)	16	4	40	24	16	856	22.0
V(III)	16	4	40	24	16	856	22.0
V(IV)	16	4	40	24	16	856	22.0
V(V)	16	4	40	24	16	856	22.0

$$E_{angle} = \frac{K_{IJK}}{2(Sin\theta_J^\circ)^2}[cos\theta_{IJK} - cos\theta_{IJK}^\circ] \tag{1}$$

$$E_{bond} = \frac{1}{2}K_{IJ}(R_{IJ} - R_{IJ}^\circ)^2 \tag{2}$$

$$E_{torsional} = \frac{V_{JK}}{2}\{1 - cos[n_{JK}(\emptyset - \emptyset_{JK}^\circ)]\} \tag{3}$$

$$E_{vdW} = D_{IJ}^0\left[\left(\frac{R_{IJ}^0}{R}\right)^{12} - 2\left(\frac{R_{IJ}^0}{R}\right)^6\right] \tag{4}$$
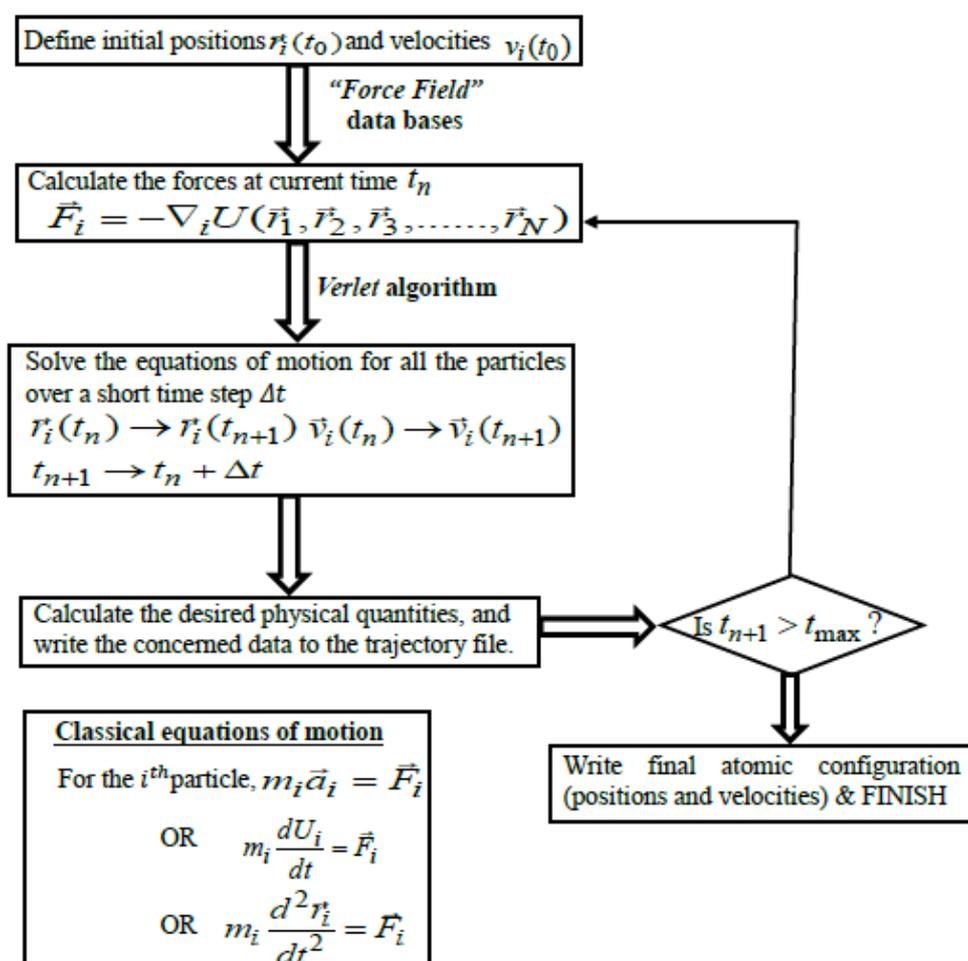
$$E_Q = \frac{q_I q_J}{4\pi\varepsilon_\circ\varepsilon R_{IJ}} \cong \frac{322.1 q_I q_J}{\in R_{IJ}} \tag{5}$$

$$U = E_{bond} + E_{angle} + E_{b\theta} + E_{OOP} + E_{torsion} + E_{vdW} + E_{ele}^{perm} + E_{ele}^{ind} \tag{6}$$

Where,

$E_{b\theta}$ = a bond angle cross term;
E_{OOP} = an out of plane bending term;

Scheme 1. Flow chart of the MD simulation

E_{vdW} = a 14–7 functional form (better than the Lennard–Jones 6–12 function);
E_{ele}^{perm} = a term for monople, dipole, and quadrupole moments; and
E_{ele}^{ind} = an induced dipole term

Similarly, the polarizable atomic multipole concepts, flexible three centered water model [23], and the five-interacting-sites models with switching function [24] are embodied for dealing with the interactions between the H_2O molecules themselves and with the H_3O^+ ions respectively. Each simulation cell hosting the particles listed in Table 1 was set to the dimensions of $100 \times 100 \times 100 \ \mathring{A}^3$, and the entire cell was annealed for about $4ns$ while establishing its equilibrium state. During this specific time period, the simulation cell was compressed to the experimental density ($\sim 1.75 \ g/cm^3$ at $300K$) plus its dimensions & the total kinetic temperature maintaining inside the system were reduced to $30\mathring{A}$ (from $100\mathring{A}$) and $300K$ (from $850K$) respectively. The visual molecular dynamics VMD graphical tools [29] were used for inspecting the annealing procedure time to time. Moreover, in the NVE ensemble, no change in number of moles (N), volume (V), and energy (E) of the system was ensured along with the constancy of the total temperature T (Nose–Hoover thermostat), total pressure P (Andersen barostat), total density D, and length of the simulation cell l explicitly. Accordingly, the total conservation of the net sum of the potential and kinetic energy of each simulating particle present in the NVE ensemble was also ensured.
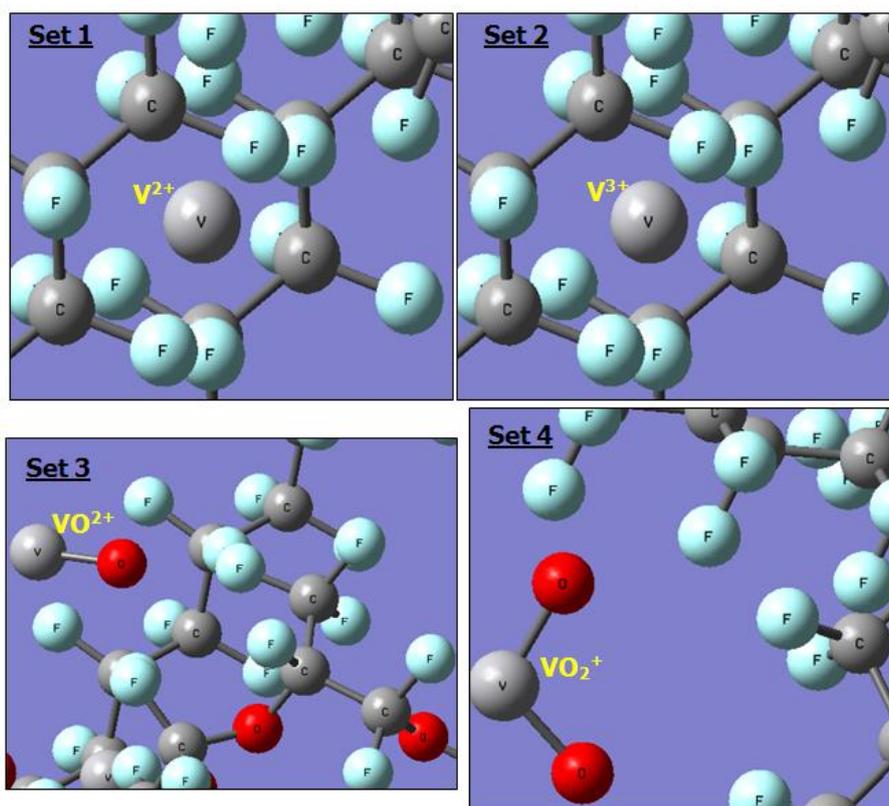
5

Fig. 1. The VMD snapshots of the four different sets of the simulation cell (dimension = 100 × 100 × 100 Å³) with the specific number of bare vanadium ions: Set 1–Vanadium (II) V^{2+} state; Set 2–Vanadium (III) V^{3+} state ; Set 3–Vanadium (IV) VO^{2+} state; and Set 4–Vanadium (V) VO_2^+ state. The rest of the molecular and ionic species present in the simulation system listed in Table 1 are excluded while snapping these rendered images

3. RESULTS AND DISCUSSION

3.1 Equilibrium States of the Simulating Systems

Since the VRFB cell system with "all-vanadium" redox couples is operated in an aqueous moderately concentrated H_2SO_4 solution, and its anolyte and catholyte solutions; V(IV)/V(V) and V(II)/V(III) states respectively; are demarcated by the Nafion type PEM (a randomly grown single polymeric form $(N_7P)_{10}$ of the Nafion−117 thread is displayed in Fig. 2), there is an occurrence of the significant diffusions of the V^{n+} ions across the membrane along with the additional particles such as H_2O, H_3O^+ (and Eigen and Zundel states of the proton), and HSO_4^- even at its ideal state. The same type diffusion is indeed more adverse at its full operational conditions or at different SOCs. Beside this, the enormous amount of protons do transport *via* the membrane through Grotthuss and /or vehicular mechanisms in the rate five times faster than the K^+ ions (H_3O^+ and

K^+ have similar ionic radii) [28,30]. Basically, in the proton transport process, the SO_3^- functional groups of the Nafion show remarkable proton exchange abilities, and the significant number of H_2O molecules absorbed in it do participate in proton transport processes through either of these two mentioned mechanisms [31(a)]. Interestingly, a wide variation in proton conductivity of the Nafion with the slight increase in its water content λ is reported: the conductivity rate is found to be increased from $0.01\,S/cm$ to $0.09\,S/cm$ whenever λ is stepped up to 22 at the rate of $\Delta\lambda = 2.5$ in an average [31(a)]. Additionally, whenever the relative humidity (RH) is changed, λ was found to be fluctuated as: (a) at $RH = 0$, $\lambda_{Nafion} \cong 1$, (b) at $RH = 100$, $\lambda_{Nafion} = 14$, and when the Nafion is dipped into the liquid water system overnight, the λ_{Nafion} is reached to 22 [31(a)]. In order to adjust this specific λ_{Nafion} value in which optimum proton conductivity of the Nafion is recorded, herein, each of the four different simulation sets (listed in Table 1) was designed with the specific number

of all the involved ionic/molecular species and the polymeric fragments. As a representative example, one of the VRFB simulation systems (Set 1) designed in the three dimensional simulation box with the cell dimension = $100 \times$ 100×100 Å^3 before and after the simulated annealing is displayed in Fig. 3, where each elongated chain surrounded by many other electrolyte particles represents an $(N_7P)_{10}$ polymeric form of the Nafion−117.
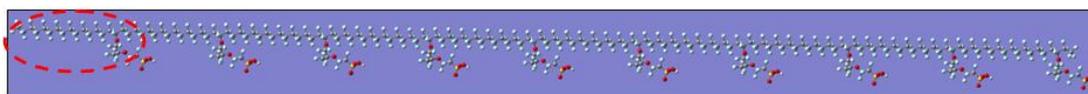

Fig. 2. A VMD rendered image of the randomly grown single $(N_7P)_{10}$ polymeric form of the Nafion−117 type membrane incorporated into the MD simulator. The four such type polymeric threads are kept into the simulation box along with many other molecular and ionic species (Table 1) so as to set the net λ_{Nafion} = 22. A single N_7P part encircled by the red dotted oval shape was replicated ten times in the course of creating this $(N_7P)_{10}$ type polymeric thread
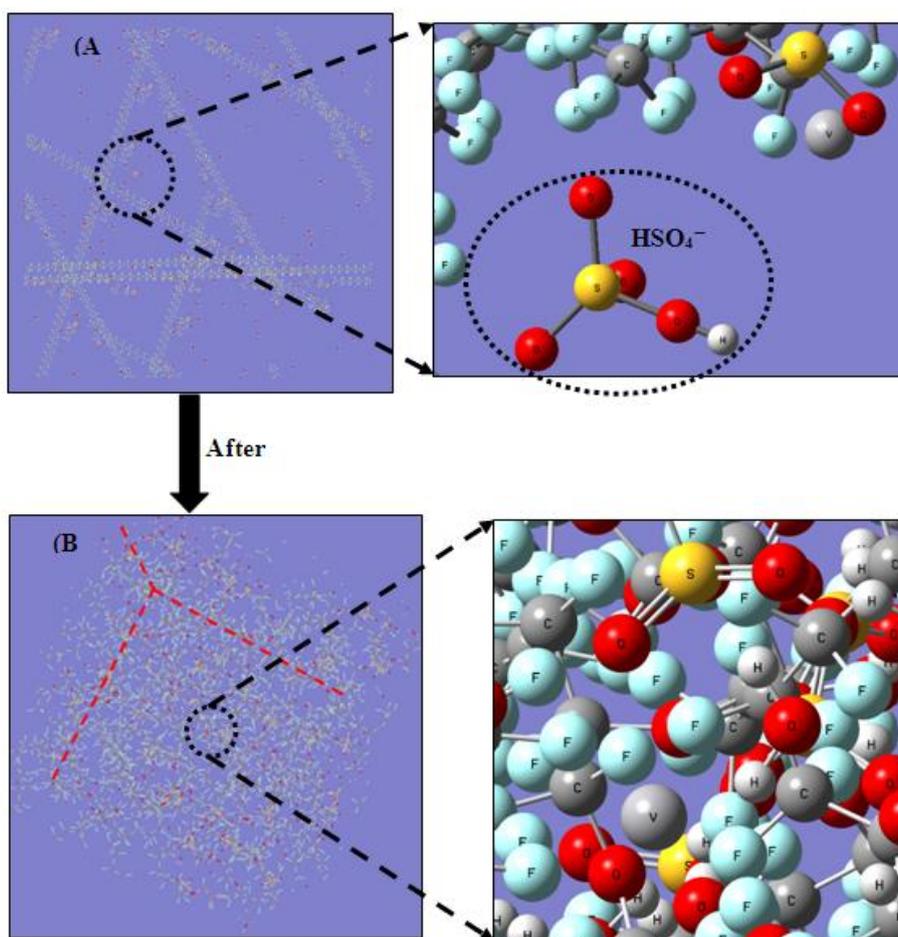

Fig. 3. A VRFB simulating system (cell dimension = $100 \times 100 \times 100$ Å^3) including all the required ionic, molecular, and $(N_7P)_{10}$ Nafion- threads (a) before annealing; (b) after annealing (the concerned image is extracted at the simulated annealing time step t = 3ns). The specific numbers of each of them suitable to satisfy the VRFB working mechanism are summarized in Table 1. The enlarged sections clarify the internal composition of the systems before and after attaining the thermodynamic equilibrium states. The HSO_4^- ion inserted into the simulator is also clearly visible, and is encircled by the oval frame. Each elongated chain in the simulation box "A" represents a $(N_7P)_{10}$ part of the Nafion
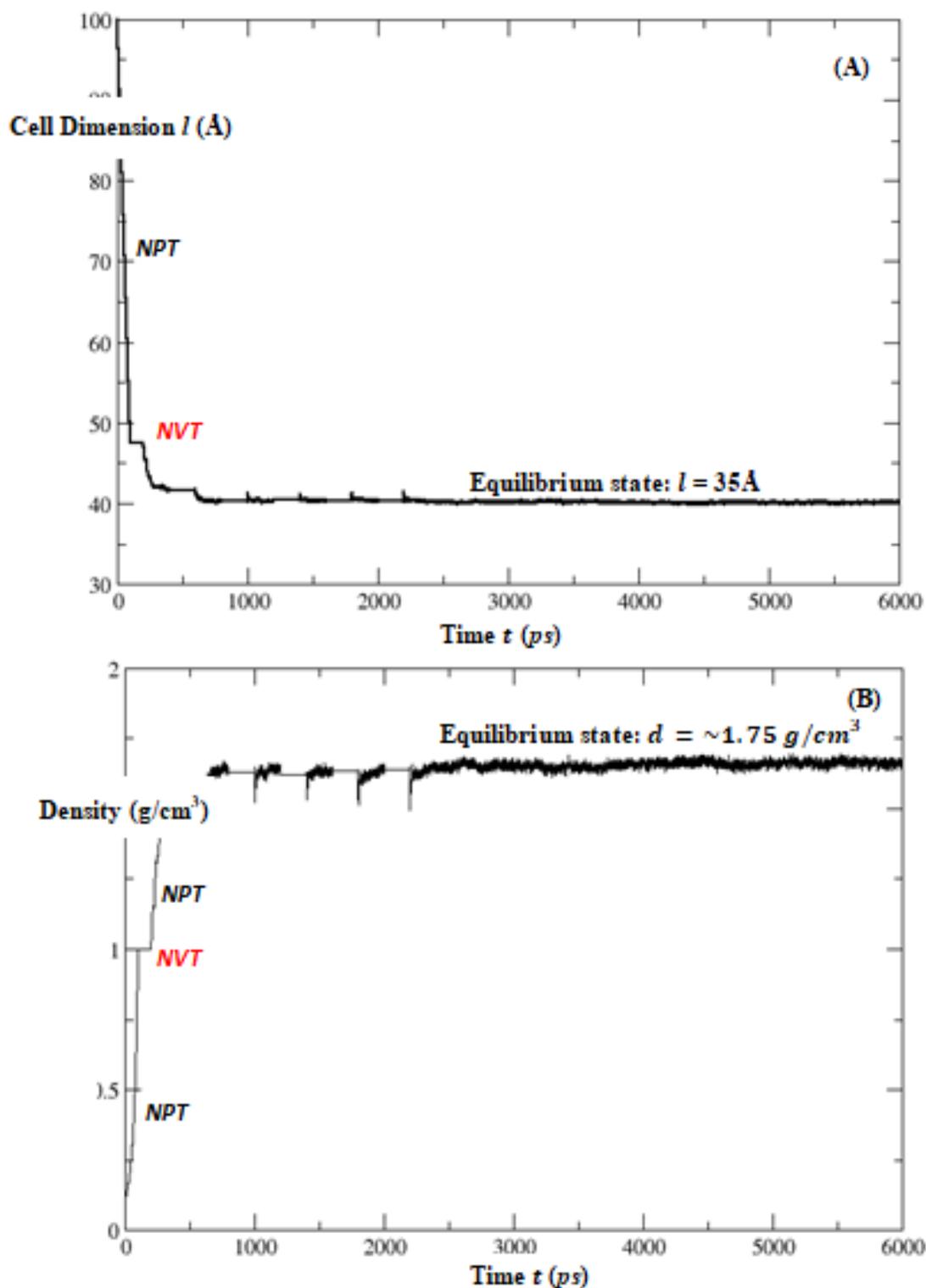
Fig. 4. A VRFB simulating system (cell dimension = 100 × 100 × 100 Å³) is compressed to the specific equilibrium parameters so as to establish the equilibrium state of the simulating system quicker. The variation in parameters such as (a) cell dimension, (b) total density, with respect to simulation time t are diagrammatically sketched. The approximate range of the iterative NPT and NVT simulations are also shown to the concerned diagrams
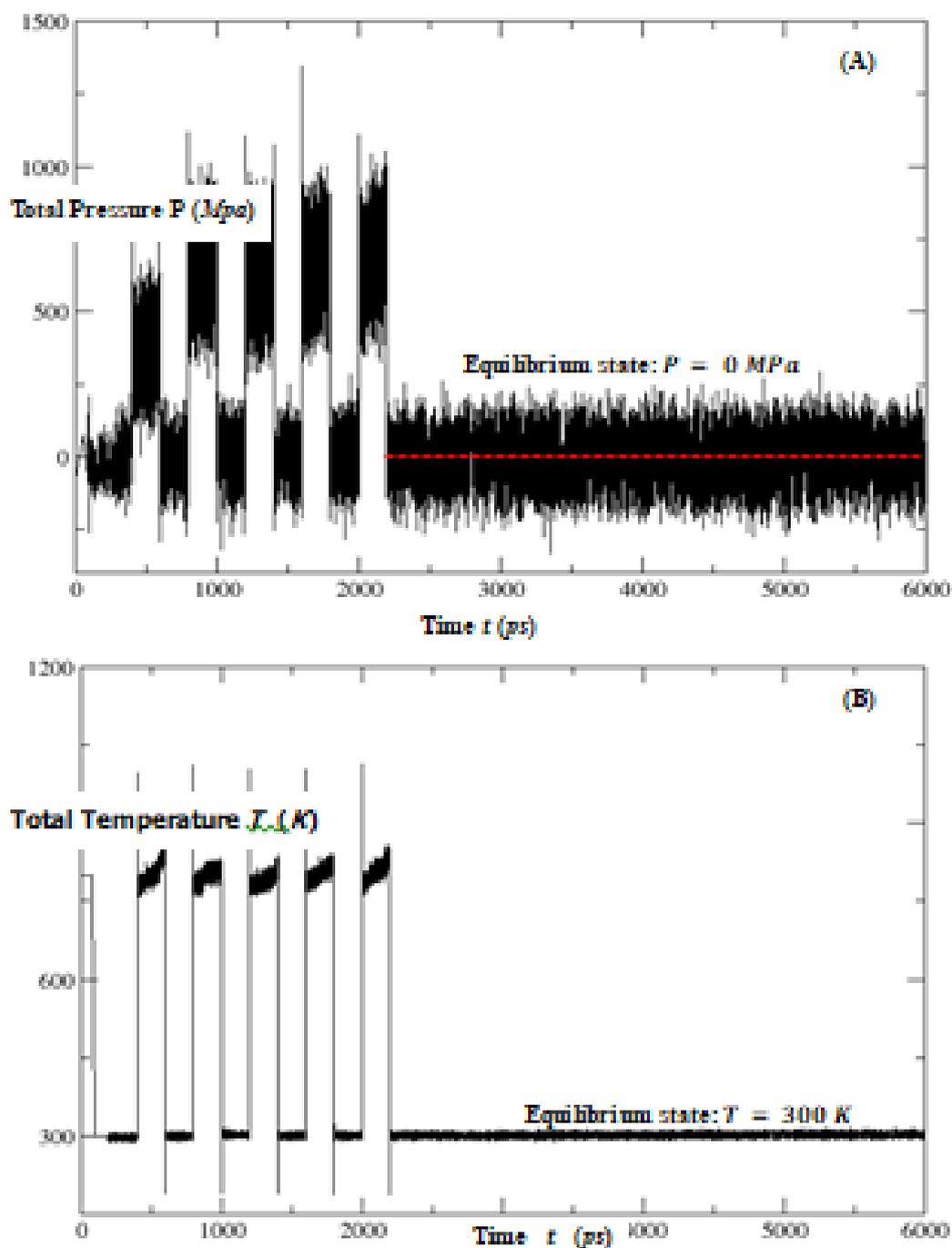
Fig. 5. A VRFB simulating system is compressed to the specific equilibrium parameters while establishing its equilibrium state. The variation in parameters (a) total pressure *P*, (b) kinetic temperature *T*, with respect to simulation time *t* are diagrammatically sketched

Since the MD simulation is a remarkable tool to predict the behavior of the chemical systems over time, the computational simulated annealing techniques referring to the effective optimization procedures of the simulating systems *via* the sufficient heating and cooling iterations, and their instant repetitions under the controlled conditions must be run in the course of establishing equilibrium states of the each simulating system. As a rule, if the cooling process is sufficiently slow, each of the simulating systems with significant number of micro particles will reach to

the global minimum (thermodynamic ensemble) faster by overcoming the energetic barriers more readily. Instead, if the rapid-cooling is employed, some irregularities in the simulation systems will be produced that not only restricts the systems in reaching to the minimum energy level but also facilitates the nucleation effects efficiently. Based on these principles, all the controlled parameters required to run several iterative series of the NPT and NVT simulations were incorporated into the VRFB−MD. The attainment of the perfect equilibrium states by maintaining all the prerequisite parameters such as length of the simulation cells l, total density of the system d, total pressure of the system P, and the total kinetic temperature T is diagrammatically illustrated in Fig. 4 and Fig. 5. The concerned change in dimension of the simulation cells (Fig. 4(A)), the change in total density of the system (Fig. 4(B)), the change in total pressure (Fig. 5 (A)), and the change in kinetic temperature of the entire simulating system (Fig. 5(B)) with respect to simulation time $t\,(ps)$ were actually derived from the annealed MD trajectory datasets. As shown in each of the respective Figure, the dimension of the simulation cell was compressed to ~$35Å$, the kinetic temperature of the ensemble was set to $300K$, and the total pressure in the system was established to $0\,Mpa$ in the course of fixing the simulation system at its equilibrium states and maintaining its equilibrium density equal to the experimentally derived value for the H−form of the Nafion−117 (experimentally derived equilibrium density = ~$1.75\,g/cm^3$ at 300 K [(31(b)]).

3.2 Radial Distribution Function (RDF $g(r)$) and Its Potential Applications

In order to simulate the larger molecular ensembles over the longer timescales, the advanced computer assisted MD simulations and their massive quantities of the trajectory datasets representing atomic Cartesian coordinates are quite mandatory tools. In fact, they create the most appropriate values of time, energy, force, temperature of the system, etc. at the specific time periods that are quite needful for the effective interpretation of the time evolution of the many− body systems. It in turn provides several time dependent thermodynamic properties such as diffusion coefficients of the ions/molecules, proton transport/hopping rate and diffusion mechanisms, solvation shell structures with solvation spheres around the ions, ion exchange tendency among the first and consecutive

solvation spheres, ion-water-PEM interactions tendencies, etc. But, the same massive MD trajectory datasets may create the substantial difficulties and tedious data-handling tasks unless they are accessed through the advanced computer aided molecular visualization & manipulation softwares, and many other rendering chemical/molecular graphics. In other words, several computer coding languages based graphical tools and many other advanced computer assisted rendering engines can only make such type data handling practically feasible, computationally convenient, physically meaningful, theoretically illuminative, scientifically predictive, and analytically informative as they enable us to render splendid views of the time evolution of the specific molecular systems and the magnificent visualizations of their closely associated temporal properties side by side [32]. Among the computationally executable externally controlled script based mathematical formulations used for handling MD derived particular type datasets and for acquiring their most essential quantitative interpretations required to elucidate many notable time−dependent physical properties of the concerned simulating systems, the most predominantly used one is the radial distribution function RDF $g(r)$; a mathematical probability density function that controls a radial variation of probability of finding any particle in a spherical shell of radius r. It is mathematically formulated as ($Eq.\,7$):

$$g_{A-B}(r) = \frac{n_B}{4\pi r^2 dr} \Big/ \frac{N_B}{V} \qquad (7)$$

Where;

$r =$ Distance between a pair of the particles;
$n_B =$ Average number of the pairs found at a distance between r and $r + dr$;
$V =$ Total volume of the system;
$N_B =$ Number of the pairs found in the whole system;

Actually, the RDF is a computationally employable and practically implementable mathematical tool that enables the scientists to calculate radial distribution functions of any reference tagged particle precisely by accessing the designated MD derived trajectories directly. Mostly, the RDF associated mathematical functions are formulated through the strategically designed programming scripts, and are executed computationally. However, in the recent days, the RDF features hosting advanced data analysis softwares and the specific image rendering molecular /chemical graphics are also used. The

visual molecular dynamics (VMD) software; a C++ programming code based computationally cheap, cost effective, and high performance visualizing three–dimensional rendering engine; is one of them. Its RDF determining tools can be linked to the MD derived gigantic trajectory datasets directly, and do access the latter straightforward in the course of acquiring required physical interpretations. The most significant advantage of using VMD's RDF features over the computer programming based RDF scripts is to retrieve many needful manipulations and visualizations of the simulating particles (molecules/ions/atoms/ fragments/polymeric membranes, etc.) in the three dimensional space explicitly [33–35], which are in fact very much essential for the exceptional assessment of these trajectory datasets. The RDF formulations implemented through either of these two computational means, and the consequent RDF plots actually stand as a quite indispensable tool for obtaining the most cost–compromise and the practically relevant quantum mechanical solutions of the giant, moderate, and small sized simulation systems set up computationally with and without periodic boundary conditions (PBC), and of their time–series trajectories. And, the VMD generated close–up graphical views of the concerned trajectories, the RDF peak positions plus the specific rendered images are extremely helpful to visualize how many atoms/ions/ molecules/ fragments, etc. fall in the particular regions, to identify the average distribution of the particles around any specific tagged particle within the system, to elucidate the time–averaged density of any constituent particles, to predict the statistical description of the local packing around any reference particles, to determine the distances between each pair of the atoms/ions/molecules/fragments, etc., and to approximate how many of such type pair distances lie into that particular sites. More importantly, the RDF based mathematical elucidations, and the chemical graphics rendered three dimensional views provide the in–depth quantitative descriptions of the hydration/ solvation/ complexation chemistry such as determination of the multiple coordination shells and the specific coordination numbers, identification of the solvation spheres and the structures around each simulating particle, investigation of the coordinating abilities of the bare transition metal ions M^{n+} with the neutral/anionic/monodentate/ polydentate type ligands, computational studies of the hydration moieties and stabilities of the aqua type complexes $[M(H_2O)_6]^{n+}$, predictions of the three dimensional metal–ligands $[M^{n+} \leftarrow L]$ spatial configurations around the central M^{n+} ion & the related geometrical parameters, etc. In the condensed–matter science, the RDF tools and the associated mathematical interpretations are highly recognized as an extremely important and quite needful measuring scale of the structures of the condensed matter, and in the liquid state & fluid sciences, they act as the most incredible descriptors for studying micro–structures of their suspended particles. More potential applications of them include investigations of the shock wave induced phase transitions in metals [36], studies of the radiation damage in nuclear waste [37] and the long range order in self–assembled monolayers [38], characterizations of the crystallinity or non-crystallinity of the solid state materials (crystalline, amorphous and nanomaterials), derivations of the interatomic distances and interatomic coordinates from the concerned X–ray diffuse type scattering patterns of the materials, predictions of the atomic structures of the disordered amorphous material [39], explorations and modeling of the macroscopic thermodynamic properties of the fluids, fluid mixtures, and their intermixing behavior, etc. [40]. Besides these, a worldwide employment of the RDF based quantitative analyses for studying battery composites, electrode materials, electrolyte compositions, polymeric membrane's proton conduction mechanisms, electrode–electrolyte interfacial structures, and many other recycling materials is remarkable [41]. Wang et al. have verified elsewhere [41] that the RDFs based mathematical formulations act as the quite essential mean for exploring micro–structural properties of the battery materials such as local structures, cation orderings, local distortions, local distributions, etc., characterizing their crystallinity or amorphous properties, and studying how electrolyte ions' immediate & consecutive structures may vary while charging and discharging of the battery, and at it's ideal states as well as at different percentage of SOCs. In particular, the RDF analyses and their direct computational implications in the problems associated with the VRFB electrochemical cell are highly expected as a benchmark theoretical mean in order to reveal the material compositions of the most potential conducting electrodes and their interfacial compositions at the nanometer range, the most immediate environment around the Nafion–117 membrane and their SO_3^- type conducting sites, the intense

affinities of the active vanadium ions (adjacent oxidation states of vanadium) towards these proton conducting sites of the membrane, the proton transporting abilities of the membrane and its internal facilitators for exhibiting facile proton diffusions, the rapid proton hopping rates between the conducting sites of the membrane, the coordinating abilities of the bare V^{n+} ions with free H_2O molecules and their hydration structures & coordination spheres, the detailed internal structures around the H_2O, H_3O^+, SO_3^-, and bare V^{n+} ions at nanometer range, etc. After all, all these RDFs associated quantitative predictions in reference to the VRFB, as presented below in Section 3.3, would be very promising theoretical results and encouraging computational/graphical clarifications required to understand the realistic working scenarios of the battery, and its internal operational conditions at different SOCs.

3.3 Internal Distribution of the VRFB-Electrolyte Particles
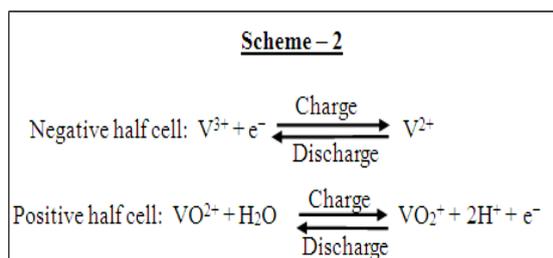
As mentioned in the introduction section, the VRFB technology is widely known for its most promising larger capacity energy storage abilities, and is preferably recognized as the renewable resources based battery candidates used for compensating the fluctuated energies in the electrical grids. So, it is accepted as the most prevailing low−cost, large−scale, grid−connected, easily recyclable, ambient temperature operational, stationary storage systems for the energy industry. It is a uniquely designed technology by utilizing the moderate H_2SO_4 solution based V(II)/V(III) couples in the negative half-cell and V(IV)/V(V) couples in the positive half-cell of the electrochemical cell. While charging, the V(IV) states loose electrons, and oxidize to V(V) but the V(III) states gain same electrons and reduce to V(II) in the positive and negative half-cells respectively, whereas the vice−versa occurs during discharging (or in the normal operation of the battery) as shown in Scheme 2. One of the contrasting features of this battery technology is to store the anolyte and catholyte solutions separately at its two different electrolyte tanks, and are pumped into the working electrochemical cell equipped with conducting electrodes and a cation exchange type Nafion−117 membrane through which H^+ ions (or its hydrated forms), H_2O molecules, HSO_4^- ions, V^{n+} ions, etc. undergo rapid exchange in between the two half-cells. Understanding the internal micro−structures of these complexities existing in the working electrolyte solutions such as V^{n+} adjacent ions' immediate & consecutive structures and their most possible internal compositional variations both at the ideal states & at different SOCs, inter-particle interactions at the molecular level, hydration shell structures around the Nafion−SO_3^- groups, each adjacent V^{n+} state, and the H_3O^+ ion, proton solvation structures nearby and/or faraway to the Nafion−SO_3^- groups (active sites), the most possible accommodation of the particles (facilitators of the proton diffusions) in between the active sites of the Nafion, etc. is really helpful for the smooth operation of the battery. The only convenient way to reveal the most trustworthy quantum mechanical solutions for them in the nanometer range is the advanced computer based molecular dynamic simulations and the RDFs based mathematical computations accessed to the MD derived trajectories. Following subchapters include the concerned theoretical findings of them explicitly with the in−depth analyses on the microstructures of each of the aforementioned VRFB electrolyte particles quantitatively.

3.3.1 Structure around the Water Molecule

The concerned RDFs plot computed over the 900 *ps* of the MD run (the number of the simulating particles present in the simulation box are tabulated in Table 1.) with the explicitly scaled specific RDF peaks is shown in Figure 6(*a*) where the mentioned terminologies O*w* and H*w* stand for the O and H atom of the H_2O molecule respectively. In the inset, the same type RDFs but in the absence of Nafion and H3O$^+$ are shown for the comparative purpose. A sharp peak of $g_{O_w-H_w(r)}$ at $r_{max} \approx 1.8\,\text{Å}$ indicates that the closed packing microstructures around the any reference H_2O molecules of the VRFB electrolytes (*aq.*) are as like as in the bulk water systems simulated without Nafion threads and H_3O^+ ions. Strictly saying, the radial distance of this first peak is exactly identical to the length of the typical hydrogen bond exists in between any

two H_2O molecules [42] as shown in the inset clearly. Similarly, another intense peak of the $g_{O_w - O_w(r)}$ appeared at the radial distance $r_{max} \approx 2.8$ Å is found to be as equal as the typical O-O distances of any two nearby H_2O molecules in the absolute aqueous environments having no Nafion and H_3O^+ ion. This radial peak position is again equal to the inter−oxygen distance of any two nearby H_2O molecules in the bulk water systems. Again, the approximate peak position of the $g_{H_w - H_w(r)}$ at $r_{max} \approx 2.4$ Å reflects that the inter−hydrogen distance in between any two nearby H_2O molecules is as equal as that in the bulk water system. The radial positions of the second highest peaks of each of the RDF plots

signify the concerned distances for the repeatedly arranged H_2O molecules in a specific periodic pattern. These comparative analyses make us to conclude that the internal micro−structures around the H_2O molecules present in the VRFB electrolyte systems do not change even after or in the course of interacting with any of its electrolyte particles viz. bare V^{n+} ions, HSO_4^- ions, H_3O^+ ions, and polymeric $(N_7P)_{10}$ type Nafion−117 threads. In other words, the nanometer range structural arrangement of the water molecules present in the aqueous VRFB electrolyte system is not significantly different to that in the purely bulk water systems.
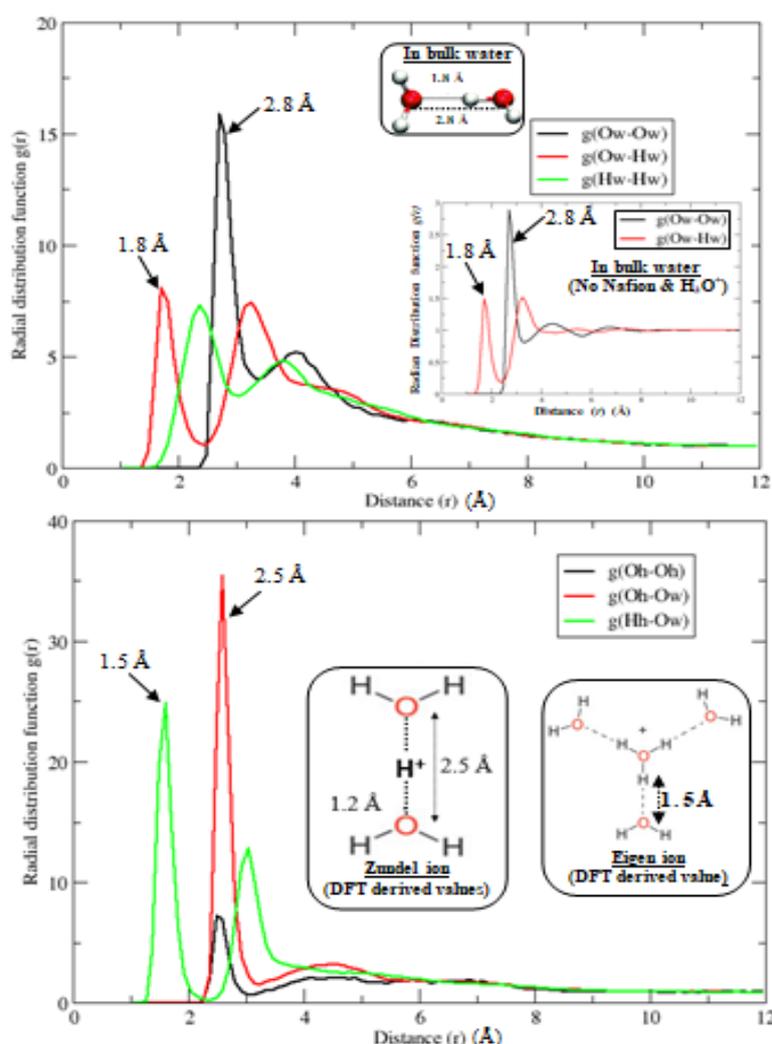

Fig. 6. The RDFs computed over the 900 *ps* of the MD run showing (a) structure around the water (H_2O) molecule (O_w = O atom, and H_w = H atom of the H_2O); (in the inset, the same type RDFs but in the absence of Nafion and H_3O^+, are shown for the comparative purpose); (b) structure around the hydronium ion (H_3O^+) (O_h = O atom, and H_h = H atom of the H_3O^+). The specific RDF peaks having the most significant physical meaning are scaled properly
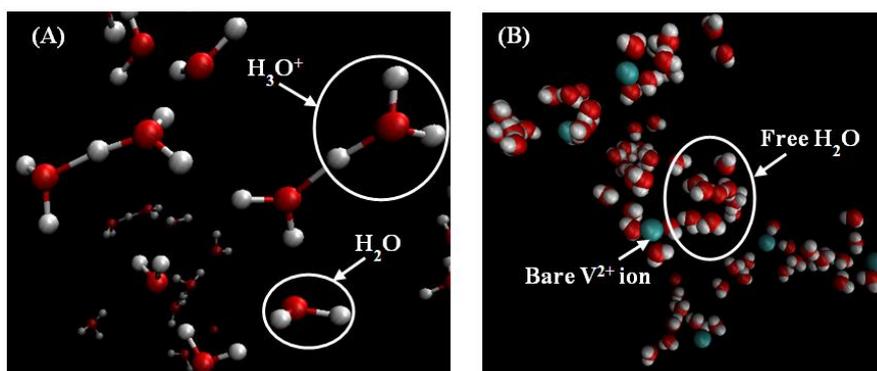
13

Fig. 7. The VMD rendered images: (a) interactions between H$_2$O and H$_3$O$^+$; reflecting H$_3$O$^+$ ionic movement (proton carrying H$_2$O) or proceeding protonic conduction in aqueous electrolyte media; (b) interactions of the bare V^{2+} ions with free H$_2$O molecules; depicting hydrated complex forming propensities of the latter ion
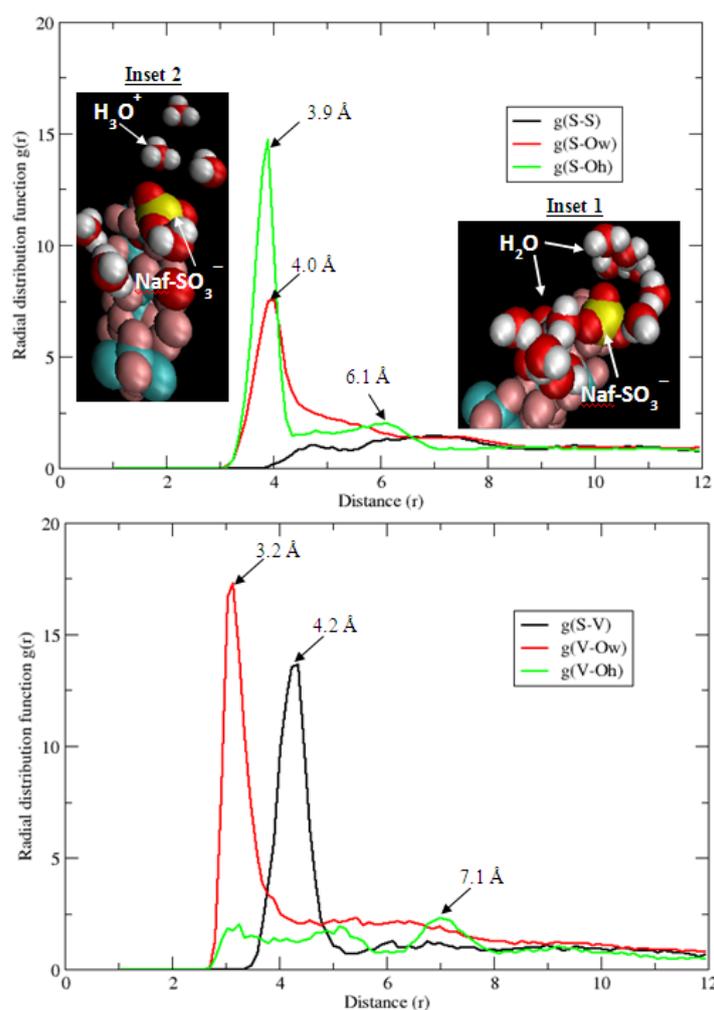

Fig. 8. The RDFs computed over the 900 *ps* of the MD run showing (a) structure around the SO$_3^-$ groups of Nafion−117 (S = S atom of the SO$_3^-$ group, O$_w$ = O atom of the H$_2$O molecule, and O$_H$ = O atom of the H$_3$O$^+$); (b) structure around the bare V^{2+} ion (V(II) oxidation state) (V = V atom in +2 oxidation state). The specific RDF peaks having the most significant physical meaning are scaled properly

3.3.2 Structure around the Hydronium Ion (H_3O^+)

The specific RDFs plot computed over the 900 *ps* of the MD run (the number of the simulating particles present in the simulation box are tabulated in Table 1) with the explicitly scaled RDF peaks is shown in Fig. 6(b) where the mentioned terminologies Ow, H$_h$, and O$_h$ stand for the O atom of H_2O, and H & O atoms of the H_3O^+ ion respectively. A sharp peak of $g_{H_h-O_w(r)}$ at $r_{max} \approx 1.5\,Å$ confirms the presence of Eigen ion $[H_9O_4]^+$ in VRFB electrolyte (*aq.*) which is actually created by the closed association of the three equivalent H_2O molecules with the centrally located H_3O^+ ion *via* the hydrogen bonding (hereafter, H−bond) whose structural alignment and the DFT derived H−bond length value (= 1.5Å) is explicitly shown in the inset [42]. Accordingly, another sharp peak of $g_{O_h-O_w(r)}$ at $r_{max} \approx 2.5\,Å$ confirms the presence of Zundel ion $[H_5O_2]^+$ formed by interlinking H^+ ion to the two equivalent H_2O molecules *via* the H−bonds whose structural alignment and the DFT derived bond distances [42] are displayed in the same inset. Both of these radial distances are exactly identical to those of the Eigen and Zundel states formed in the bulk water systems simulated without V^{n+}, HSO_4^-, & H_3O^+ ions, and polymeric $(N_7P)_{10}$ type Nafion −117 threads. These distributions and radial position analyses reflect that the internal structure around the protonated water *i.e.* H_3O^+ ionic state present in the VRFB system does not change even after or in the course of interacting with the bare V^{n+} ions, HSO_4^- ions, H_3O+ ions, and polymeric Nafion−117 type threads. This quantitative detection of these complex states of the proton in the VRFB electrolyte (*aq.*) system reflects that there is a presence of the sufficient amounts of H_3O^+ ions, but remain there in the dynamical form which is in fact a theoretical verification for stressing "proton conduction in the aqueous VRFB electrolyte (*aq.*) system is promptly proceeded through the involvement of H_3O^+ ions either in the Grotthuss or in the vehicular type diffusion pathways" as demonstrated by the VMD rendered images displayed in Fig. 7(A).

3.3.3 Structure around the Nafion-SO_3^- groups (Active Centers)

The RDFs plot computed over the 900 *ps* of the MD run (the number of the simulating particles present in the simulation box are tabulated in Table 1) with the specific RDF peaks is shown in Fig. 8(a) where the mentioned terminologies: *S* represents an S atom of the SO_3^- group, O_w is for an O atom of the H_2O molecule, and O_H stands for the O atom of the hydronium H_3O^+ ion. A diffuse type distribution pattern of $g_{S-S(r)}$ expanded over the radial distance $r \geq 4.0\,Å$ confirms the widely dispersed distribution of the SO_3^- groups in Nafion−117, and the maximum number density of SO_3^- around any other reference SO_3^- group is only available in between $6\,Å$ to $8Å$. This quantitative prediction supports the fact that whenever the water content λ of the Nafion−117 type membrane is maximum (in this case, $\lambda = 22$), it swells sufficiently (swelling ratio at $\lambda = 20$ is reported as 30 [43]) resulting an increase in size of the aqueous domain; means the significant departures of the SO_3^- groups to each other takes place leading to the elongation in the S-S distances of the any two SO_3^- groups which is actually called a "peak shifting" taking place from very original radial positions; S-S radial position of the peak assigned to the protonated & very dry Nafion is shorter than that to the deprotonated & wet Nafion due to having no proton conducting water channels in between its active SO_3^- centers. A sharp peak of $g_{S-O_w(r)}$ appeared at $r_{max} \approx 4.0\,Å$ explains the most probable position for finding the maximum number density of H_2O around the vicinity of any reference SO_3^- groups of the Nafion−117, and the non-zero value of the same RDF after $4.2\,Å$ radial distance describes the inhomogeneously distributed H_2O molecules at the *nm* range (a VMD rendered magnificent image showing the closed interactions between the SO_3^- and H_2O is shown in the Inset 1). A relatively narrower peak of the $g_{S-O_h(r)}$ appeared at $r_{max} \approx 3.9\,Å$ assures that an intense accumulation of the H_3O^+ ions at the immediate surrounding of the SO_3^- groups takes place (a VMD rendered graphical view showing the closed association of the H_3O^+ ions around the periphery of SO_3^- is shown in the Inset 2), and the first minimum appeared at a radial distance $\sim 4.3\,Å$ approximates the region where the first solvation shell boundary is terminated. The shifting in a peak position relatively more towards the shorter radial distance value in $g_{S-O_h(r)}$ is due to the opposite charge carried by the SO_3^- and H_3O^+ species which actually make the latter crowded very near to the former one. A non-zero value of the $g_{S-O_h(r)}$ & $g_{S-O_w(r)}$ distributed in between the two peaks positioned at $\sim 3.9\,Å$ and $\sim 6.1\,Å$ indicates the existence of utmost possibility of transferring proton and exchanging H_2O molecules between

the SO_3^- groups of the Nafion. Nevertheless, the appearance of the diffuse type $g_{S-S(r)}$ peak for the SO_3^- groups of Nafion above 5Å radial distance signifies that there is a presence of enough amount of free space in between any two SO_3^- groups even at the equilibrium state where the sufficient number of free H_2O molecules and the hydrated protons (H_3O^+ ions) can be accommodated (Scheme 2), which in fact is very much essential in order to facilitate the proton hopping process taking place throughout the water channel of the deprotonated Nafion membrane this in turn is extremely needful to enhance its proton conduction and ionic mobility rates under the wet conditions (high water content λ): one of the indispensable provisions for achieving a remarkable operational performance of the VRFB–PEM based electrochemical cells. Just for the reference, the proton conductivity (σ) rate in the deprotonated Nafion at a higher water content λ reported elsewhere [44] is underscored here as $\sigma \cong 100 mScm^{-1}$: this exceptionally higher conduction rate is only attained whenever the interstitial H_2O and H_3O^+ species (the major constituents of the Nafion's water channel) inhibiting in between any two SO_3^- units of the Nafion participate in proton transportation/ diffusion processes.
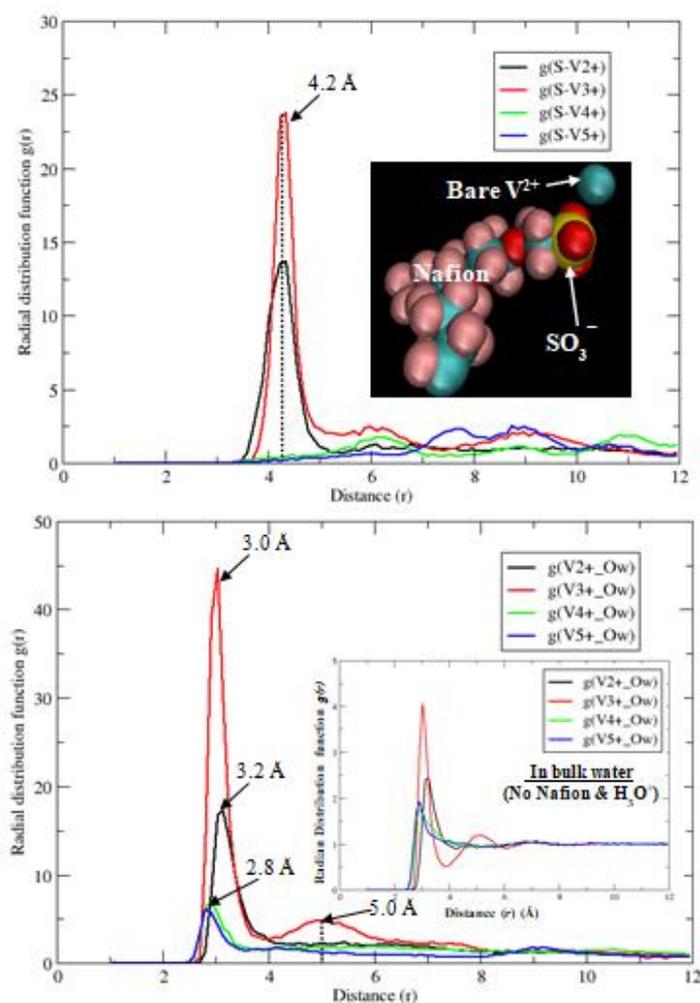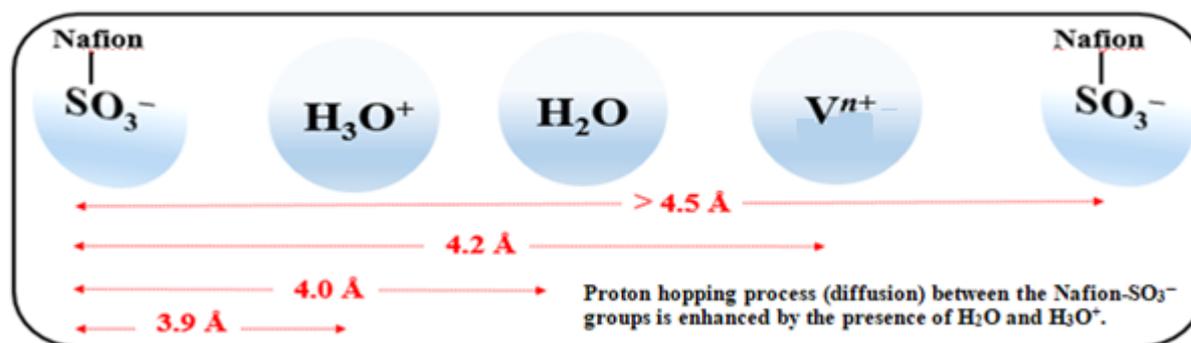

Fig. 9. The RDFs computed over the 900 *ps* of the MD run showing (a) structure around the bare V^{n+} adjacent oxidation states in reference to SO$_3^-$ groups of Nafion–117 (S = S atom of the SO$_3^-$ group; (b) structure around the bare V^{n+} states in reference to H$_2$O (O$_w$ = O atom of the H$_2$O molecule) (in the inset, the same type RDFs but in the absence of Nafion and H$_3$O$^+$ are shown for the comparative purpose). The specific RDF peaks having the most significant physical meaning are scaled properly

Scheme 2. Summary of the RDF-derived Radial distances between the VRFB electrolyte particles

3.3.4 Structure around the Adjacent Bare Vanadium Ions (V^{n+})

The concerned RDFs plots computed over the 900 *ps* of the MD run (the number of the simulating particles present in the simulation box are tabulated in Table 1) with the explicitly scaled RDF peaks are shown in Fig. 8(b), Fig. 9(a), and Fig. 9(b) where the mentioned terminologies: *S* represents an S atom of the SO_3^- group, O_w signifies an O atom of the H_2O molecule, O_h stands for the O atom of the H_3O^+ ion, S–V^{n+} and V^{n+}–O_w stand for the interactions between the SO_3^- & adjacent V^{n+} ions, and adjacent V^{n+} & H_2O respectively. As shown in Fig. 8(b), a diffused distribution diagram of the $g_{V-O_h(r)}$ with a broad spectrum appeared at a quite long radial distance ($\cong 7.1\,\text{Å}$) is because of the strong electrostatic repulsions between the V^{n+} and H_3O^+ ions due to having intense positive charges. But, the sharp peaks of $g_{S-V^{n+}(r)}$ appeared at 4.2 Å region (Fig. 9(a)) from any SO_3^- group of the Nafion are due to the stronger electrostatic force of attractions (oppositely charged species) between the adjacent V^{n+} ions and the Nafion–SO_3^- groups which actually enlightens the most probable site where the maximum number density of +2 and +3 states of vanadium *viz.* V^{2+} & V^{3+} are available. In the same diagram, the concerned RDF peaks of the $g_{S-V^{n+}(r)}$ for the V^{4+} and V^{5+} states of vanadium (oxovanadium ions) *viz.* VO^{2+} & VO_2^+ are found to be dispersed relatively very widely, and are located farther than the V^{2+} & V^{3+} states from the Nafion-SO_3^- groups. This variation in the radial distributions is because of the repulsive forces experienced by the negative poles of each VO^{2+} & VO_2^+ ion and the SO_3^- units [45]: the two oppositely charged poles at vanadium (positive pole) and oxygen (negative pole) terminals in each VO^{2+} & VO_2^+

ion (Scheme 3) are actually developed due to the significant electronegativity differences ($\Delta\chi$) between the Oxygen ($\chi O = 3.44$ in Pauling scale) and the Vanadium ($\chi V = 1.63$) atoms. Moreover, the intense peaks of the $g_{V^{2+}-O_w(r)}$ appeared at the radial distance 3.2 Å (Fig. 9(b)), and of the $g_{V^{3+}-O_w(r)}$ appeared at 3.0 Å approximate the V–OH_2 bond lengths of the respective stable hydrated complexes $[V(H_2O)_6]^{2+}$ & $[V(H_2O)_6]^{3+}$ with the free H_2O molecules in the equilibrium state (low energy ground states). And, the similar type peaks but relatively low height appeared at the smaller distances 2.8 Å and 2.6 Å for the $g_{V^{4+}-O_w(r)}$ and $g_{V^{5+}-O_w(r)}$ distribution indicates the backward shifting of the respective RDF peaks. This quantitative observation reflects that the hydrated complexes of the vanadium in tetravalent and pentavalent states; $[VO(H_2O)_4]^{2+}$ and $[VO_2(H_2O)_5]^+$ must have the shorter V–OH_2 bond distances (than in the divalent $[V(H_2O)_6]^{2+}$ and trivalent $[V(H_2O)_6]^{3+}$ aqua complexes) as predicted by the *ab initio* based DFT calculations reported elsewhere [46,47] by the same author. The concerned values in the Angstrom (Å) scale are reproduced here as well, and summarized in Table 2 for the comparative purpose. Furthermore, the relatively shorter heights and the smaller areas of the peaks assigned to the $g_{V^{4+}-O_w(r)}$ and $g_{V^{5+}-O_w(r)}$ radial distributions signify that the V^{4+} and V^{5+} states may form the respective stable aqua complexes with low hydration numbers (n), *viz.* $n = 4$ and 5 as confirmed by the DFT:B3LYP based quantum mechanical method. Their comparatively less n value in fact is because of the presence of one and two oxygen atoms in their respective stable oxovanadium cationic forms. Again, a good resemblance of the RDF peak positions and the heights of each concerned peak of $g_{V^{n+}-O_w(r)}$ in

the bulk water system having no Nafion, H_3O^+, and HSO_4^- ions (as shown in the inset of Fig. 9(b)) with those calculated in the VRFB system supports the fact that there is no significant change in inter–particle interactions between the central V^{n+} & the peripheral H_2O (V–OH_2 interactions) and the substantial variations of the bare adjacent states V^{n+} ions' affinities towards complexing with the free H_2O molecules in either of the systems. If the hydration shells around the each bare V^{2+}/V^{3+} and VO^{2+}/VO_2^+ ions are analyzed closely, the first minima are found in the range at $3.8\,\text{Å}$, and $3.2\,\text{Å}$ respectively; approximating the boundaries for the first hydration/solvation shell quantitatively. Similarly, a closed inspection of the RDF $g_{V^{n+}-O_{w(r)}}$ peak values for the V^{2+}, V^{3+}, & VO^{2+} states (VO_2^+ state) and their respective DFT derived V–OH_2 bond lengths reveals that a relatively larger (smaller) deviations are seen in the values assigned to the former. This might be due to the intense (mild) polarizing abilities of their high (reasonable) atom-centered charge density to the surrounding water molecules [45] as it is based on the fact that the direct polarizing power or the induced one is directly proportional to the charge density of the targeted ions. In the current VRFB MD simulator, this type adverse effect was unable to address fully due to the lack of proper force fields and the corresponding databases. Strictly writing, the trivalent oxidation states of vanadium V^{3+} shows the strongest polarization effect to the surrounding H_2O molecules due to having relatively the highest atom-centered charge density which in fact causes the latter to depart farther from the former, and behaves uniquely: as shown in Fig. 9(b), unlike other states of the vanadium, the V^{3+} ions start forming a second hydration shell (from $\cong 4.0\,\text{Å}$ region) immediately after the completion of the first one at $\cong 3.8\,\text{Å}$ region, and initiate gathering a maximum number density of H_2O molecules again at $\cong 5.0\,\text{Å}$ region. Additionally, the $g_{V^{n+}-rad(r)}$ peak positions appeared at the radial distance greater than $3.5\,\text{Å}$ (Fig. 10) indicate that the HSO_4^- radicals (*rad*) maintain relatively longer distance with the V^{n+} ions at equilibrium state despite having opposite charge in them. It further means that the HSO_4^- radicals have almost no chance of making new complexes with the V^{n+} ions, which is a good evidence of not involving the former in trapping (leading to the wastage of the active V^{n+} ions) as well as in obstructing the conduction process of the latter.
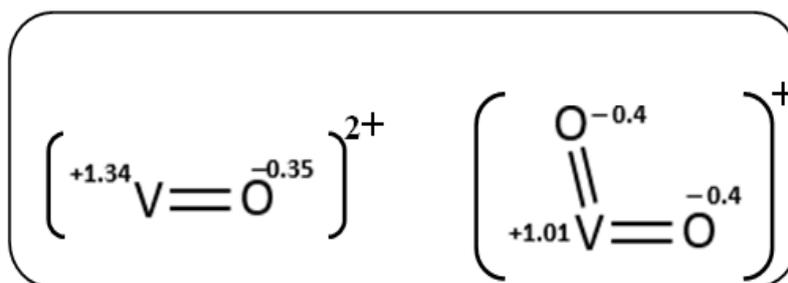
Scheme 3. Polarity in the Oxovanadium Ions

Table 2. Comparison of the MD trajectories based RDF peak positions and the *ab initio* based DFT derived bond lengths [44]

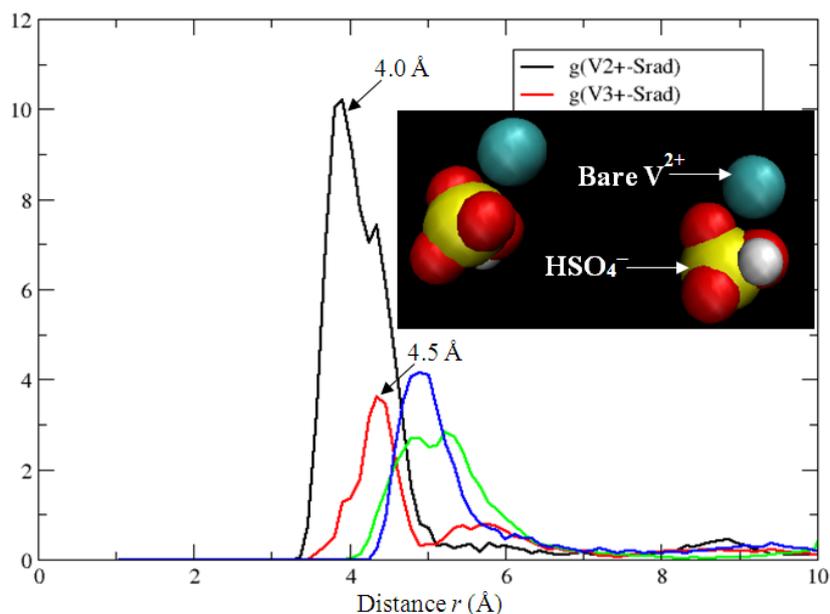| Simulation sets/ Vanadium ions	MD trajectories based RDF peak positions (Å)		*Ab initio* based DFT calculations	
	VRFB system	Bulk water system	V–OH_2 bond length (Å)	Hydration number (*n*)
Set–1: V^{2+}	3.2	3.2	2.4	6
Set–2: V^{3+}	3.0	3.0	2.0	6
Set–3: VO^{2+}	2.8	2.8	2.1	5
Set–4: VO_2^+	2.6	2.8	2.1	4

Fig. 10. The RDFs computed over the 900 *ps* of the MD run showing (a) structure around the bare V^{n+} adjacent oxidation states in reference to HSO_4^- radical where S_{rad} represents an S atom of the HSO_4^- radical. In the inset, the VMD rendered graphical views illuminating the closed interactions between the HSO_4^- radical and bare V^{n+} ions are displayed. The concerned RDF peaks (black and red lines) associated with the V^{2+} and V^{3+} states are scaled properly. The blue and green lines are excluded here

4. CONCLUSION

Being Vanadium Redox Flow Battery (VRFB) technology the most attractive energy storage candidate in the renewable energy sectors worldwide simply due to its ability of converting chemical energy into the electrical energy by utilizing "all–vanadium" redox couples as its electroactive chemical materials, understanding internal micro-structures around the Nafion fragments, Sulphur centered HSO_4^- ions, adjacent states V^{n+} ions, hydrated protons (H_3O^+), etc. present in its moderate H_2SO_4 (*aq.*) based electrolyte matrix of the V^{n+} electrolytes at the molecular level plus their explicit key roles in enhancing battery performance and in the betterment of its normal functionalization is indispensable as they are directly associated with the typical operational mechanisms of the battery both at its ideal as well as different States of Charges (SOCs). In this regard, this research report stands as a doctrine article where the additional explicit explanations required to address some of the specific VRFB–cell operational issues such as: interfacial distribution of the V^{n+}, H_2O, and H_3O^+ around the Nafion–SO_3^- conducting sites, and their intense affinities towards the latter; internal facilitators for enhancing proton conduction rate of the

Nafion; coordinating ability of the bare V^{n+} ions with free H_2O & their hydration shell structures, etc. are presented. Towards disclosing very reliable yet quantitative facts related to them, one of the most efficient, versatile, and quantum mechanically esteemed theoretical mean; Molecular Dynamics (MD) simulation method; was employed computationally by incorporating all the prerequisite forcefield databases, mathematical formulations, & force constants of the interaction potentials, computational algorithms, annealed simulation constraints, etc. required to cope with the internal working mechanism of the VRFB-cell and its electrolyte compositions. The Radial Distribution Functions (RDF) based mathematical formulations & their executable computer programming script were used to access all the MD derived trajectory datasets explicitly and to acquire all the associated quantitative interpretations.

The general results showed that (a) the structural arrangement of the water molecules present in the VRFB electrolyte (*aq.*) system is not significantly different to that in the purely bulk water systems; (b) the dynamic type complex states of the proton; Hydronium (H_3O^+), Eigen ($H_5O_2^+$), and Zundel ($H_9O_3^+$); detected in the VRFB electrolyte (*aq.*) depict their direct

involvement in either Grotthuss or vehicular type proton conductions pathways; (c) the SO_3^- conducting units of the wet Nafion (at water content, λ = 22) that were found to be departed to each other in a greater extent even at the equilibrium state confirms its ability of easy accommodating sufficient number of free H_2O molecules and H_3O^+ ions as internal facilitators for exhibiting efficient conduction; strengthening its experimentally observed exceptionally high proton conductivity and ionic mobility rates in wet conditions; (d) no significant change in inter−particle interactions between the central V^{n+} & the peripheral H_2O (V−OH_2 interactions), and in the variations of the bare adjacent states V^{n+} ions' affinities towards complexing with the free H_2O molecules plus their hydration (coordination) numbers are observed in VRFB system with Nafion fragments, H_2O, H_3O^+, and HSO_4^- ions, and purely bulk water system without them except in the hydration spheres, and inter−solvation shell water exchange probabilities. However, the RDFs derived peak positions for the $V^{n+}-$ H_2O interactions are found to be deviated from the concerned DFT: B3LYP derived V−H_2O bond lengths (the significant deviation was observed in the simulation system with V^{3+} ions). But, this was interpreted as a quite obvious results as the atom−centered charge density of all the adjacent V^{n+} states impose intense polarizations to the surrounding water molecules whose adverse effects were unable to address fully in the current VRFB based MD simulator due to the lack of proper databases and suitable forcefield packages.

ACKNOWLEDGEMENT

COMPETING INTERESTS

Author has declared that no competing interests exist.

REFERENCES

1. Madan RD. Modern Inorganic Chemistry, S. Chand & Company Ltd.: New Delhi; 1997.

2. Krakowiak J, Lundberg D, Persson I, A Coordination Chemistry Study of Hydrated and Solvated Cationic Vanadium Ions in Oxidation States +III, +IV, and +V in Solution and Solid State, Inorg. Chem. 2012;51(18):9598–9609. Available:https://pubs.acs.org/doi/full/10.1021/ic300202f

3. Persson I. Hydrated metal ions in aqueous solution: How regular are their structures? Pure Appl. Chem. 2010; 82(10):1901–1917. Available:https://publications.iupac.org/pac/82/10/1901/index.html

4. Yamamura T, Marahatta AB, Yoshida S, Tanno N, Vanadium Redox Flow Battery, WIPO (PCT) Patent WO2016158295A1; 2016. Available:https://patents.google.com/patent/WO2016158295A1/ru

5. Yamamura T, Marahatta AB, Yoshida S, Tanno N, Vanadium Redox Flow Battery, Japan Patent JP2016186853A; 2015. Available:https://patents.google.com/patent/JP2016186853A/ja

6. Mukherjee B, Patra B, Mahapatra S, Banerjee P, Tiwari A, Chatterjee M, Vanadium-an element of atypical biological significance, Toxicology Letters. 2004; 150(2):135-143. Available:http://www1.udel.edu/chem/polenova/VHPO/Vanadium_BIolSignif_ToxicLett2004.pdf

7. Rowley AF. The blood cells of the sea squirt, Ciona intestinalis: Morphology, differential counts, and in vitro phagocytic activity, J. Inv. Pathology. 1981; 37(1): 91-100. Available:https://www.sciencedirect.com/science/article/abs/pii/0022201181900604

8. Pessoa JC, Etcheverry S, Gambino D, Vanadium compounds in medicine, Coord. Chem. Rev. 2015; 301:24-48. Available:https://www.ncbi.nlm.nih.gov/pmc/articles/PMC7094629/

9. Bishayee A, Waghray A, Patel MA, Chatterjee M, Vanadium in the detection, prevention and treatment of cancer: the in vivo evidence, Cancer Lett. 2010; 294 (1):1-12. Available:https://pubmed.ncbi.nlm.nih.gov/20206439/

10. Bhattacharya PK, Water flooding in the proton exchange membrane fuel cell, Directions. 2015;15(1): 24-33.
Available:https://www.sciencetheearth.com/uploads/2/4/6/5/24658156/waterfloodingprotonexchangemembrane.pdf

11. Kurbatova LD, Kurbatov DI, Vanadium (V) complexes in Sulfuric Acid Solutions, Russ. J. Inorg. Chem. 2006; 51: 841–843.
Available:https://link.springer.com/article/10.1134/S0036023606050275

12. Nechay BR, Mechanisms of Action of Vanadium, Ann. Rev. Pharmacol. Toxicol. 1984;24:501-524.
Available:https://www.annualreviews.org/doi/abs/10.1146/annurev.pa.24.040184.002441

13. Rehder D, The coordination chemistry of vanadium as related to its biological functions, Coord. Chem. Rev. 1999;182(1):297−322.
Available:https://www.sciencedirect.com/science/article/abs/pii/S0010854598001945

14. Vijayakumar M, Li L, Graff G, Liu J, Zhang H, Yang Z, Hu JZ, Towards understanding the poor thermal stability of V^{5+} electrolyte solution in Vanadium Redox Flow Batteries, J. Pow. Sources 2011; 196(7): 3669-3672.
Available:https://www.sciencedirect.com/science/article/abs/pii/S0378775310021178

15. Marahatta AB, Coordination Chemistry of Vanadium Aquo Complex Ions in Oxidation States +II, +III, +IV, and +V: A Hybrid-Functional DFT Study, Int. J. Prog. Sci. Tech. 2020; 24(1): 645-661.
Available:https://ijpsat.org/index.php/ijpsat/article/download/2496/1543

16. Marahatta AB, DFT Study on Electronic Charge Distribution and Quantum−Chemical Descriptors for the Kinetic Stability of Vanadium Aquo Complex Ions $[V(H_2O)_6]^{2+}$ and $[V(H_2O)_6]^{3+}$, Int. J. Prog. Sci. Tech. 2020;22(1): 67−81.
Available:https://ijpsat.org/index.php/ijpsat/article/view/2006/1132

17. Marahatta AB, Towards Understanding the Stabilities of Hydrated Vanadium (V) Complex Ions and the Pathway of V_2O_5 Precipitation in Catholyte Solution of Vanadium Redox Flow Battery, Int. J. Prog. Sci. Tech. 2020;20(2): 348−364.
Available:https://ijpsat.org/index.php/ijpsat/article/view/1805/1020

18. Bühl M, Kabrede H, Geometries of Transition-Metal Complexes from Density-Functional Theory, J. Chem. Theory Comput. 2006;2(5):1282-1290.
Available:https://pubs.acs.org/doi/abs/10.1021/ct6001187

19. Allinger NL, Conformational analysis. 130. MM2. A hydrocarbon force field utilizing V1 and V2 torsional terms, J. Am. Chem. Soc. 1977; 99(25):8127− 8134.
Available:https://pubs.acs.org/doi/10.1021/ja00467a001
(b) Sprague JT, Tai JC, Yuh Y, Allinger NL, The MMP2 calculational method, J. Comput. Chem. 1987; 8:581–603.
Available:https://onlinelibrary.wiley.com/doi/10.1002/jcc.540080504

20. (a) Weiner SJ, Kollman PA, Case DA, Singh UC, Ohio C, Algona G.; Profeta Jr. S, Weiner PJ, A Study of thermal decomposition in cellulose by molecular dynamics simulation, Am. Chem. Soc. 1984; 106:765–784.
Available:https://www.scirp.org/(S(351jmbntvnsjt1aadkposzje))/journal/paperinformation.aspx?paperid=503
(b) Weiner SJ, Kollmann PA, Nguyen DT, Case DA, An all atom force field for simulations of proteins and nucleic acids, J. Comput. Chem. 1986; 7(2):230–252.
Available:https://pubmed.ncbi.nlm.nih.gov/29160584/

21. Mayo SL, Olafson BD, Goddard WA, DREIDING: A Generic Force Field for Molecular Simulations, J. Phys. Chem. 1990; 94:8897−8909.
Available:http://dx.doi.org/10.1021/j100389a010

22. Ponder JW, Wu C, Ren P, Pande VS, Chodera JD, Schnieders JM, Haque I, Mobley LD, Lambrecht SD, DiStasio AR, Gordon MH, Clark GNI, Johnson ME, Gordon HT, Current Status of the AMOEBA Polarizable Force Field, J. Phys. Chem. B. 2010; 114(8): 2549–2564.
Available:https://pubmed.ncbi.nlm.nih.gov/20136072/

23. Ren P, Ponder JW, Polarizable Atomic Multipole Water Model for Molecular Mechanics Simulation, J. Phys. Chem. B. 2003;107(24): 5933–5947.
Available:https://pubs.acs.org/doi/abs/10.1021/jp027815+

24. Levitt M, Hirshberg M, Sharon R, Laidig KE, Daggett V, Calibration and Testing of a

Water Model for Simulation of the Molecular Dynamics of Proteins and Nucleic Acids in Solution, J. Phys. Chem. B 1997; 101(25): 5051-5061. Available:https://doi.org/10.1021/jp964020s

25. Walbran S, Kornyshev AA, Proton transport in polarizable water, J. Chem. Phys. 2001;114:10039-10048. Available:https://aip.scitation.org/doi/10.1063/1.1370393

26. Spreiter Q, Walter M, Classical Molecular Dynamics Simulation with the Velocity Verlet Algorithm at Strong External Magnetic Fields, J. Comp. Phy. 1999; 152(1):102-119. Available:https://www.sciencedirect.com/science/article/pii/S002199919996237X

27. Martys NS, Mountain RD, Velocity Verlet algorithm for dissipative-particle-dynamics-based models of suspensions, Phys. Rev. E 1999;59(3): 3733–3736. Available:https://journals.aps.org/pre/abstract/10.1103/PhysRevE.59.3733

28. Grubmüller H, Heller H, Windemuth A, Schulten K, Generalized Verlet Algorithm for Efficient Molecular Dynamics Simulations with Long-range Interactions, Molecular Simulation 1991; 6:121-142. Available:https://www.tandfonline.com/doi/abs/10.1080/08927029108022142

29. Dorenbos G, Suga Y, Simulation of equivalent weight dependence of Nafion morphologies and predicted trends regarding water diffusion, J. Memb. Science 2009; 330(1-2):5-20. Available:https://www.sciencedirect.com/science/article/abs/pii/S0376738808010119

30. Humphrey W, Dalke A, Schulten K, VMD: visual molecular dynamics, J. Mol. Graph. 1996; 14(1):33(8):27-8. Available:https://pubmed.ncbi.nlm.nih.gov/8744570/

31. (a) Jang SS, Molinero V, Çağın T, Goddard WA, Nanophase-Segregation and Transport in Nafion 117 from Molecular Dynamics Simulations: Effect of Monomeric Sequence, J. Phys. Chem. B 2004; 108(10): 3149–3157. Available:https://pubs.acs.org/doi/abs/10.1021/jp036842c
(b) Karo J, Aabloo A , Thomas JO, Brandell D, Molecular Dynamics Modeling of Proton Transport in Nafion and Hyflon Nanostructures, J. Phys. Chem. B 2010; 114:6056–6064

Available:https://pubs.acs.org/doi/10.1021/jp903288y

32. Hsin J, Arkhipov A, Yin Y, Stone JE, Schulten K, Using VMD: An Introductory Tutorial, Current Protocols in Bioinformatics 2008; 5.7.1–5.7.48. Available:https://pubmed.ncbi.nlm.nih.gov/19085979/

33. Marahatta AB, Advanced Computer Graphics Aided Molecular Visualization And Manipulation Softwares: The Hierarchy of Research Methodologies, Int. J. Prog. Sci. Tech. 2023; 36(2):136–160. Available:https://ijpsat.org/index.php/ijpsat/article/view/4756New

34. Hildebrand PW, Rose AS, Tiemann JKS, Bringing Molecular Dynamics Simulation Data into View, Trends Biochem. Sci. 2019; 44(11):902–913. Available:https://pubmed.ncbi.nlm.nih.gov/31301982/

35. VMD User's Guide (version 1.9.3); 2016. Available:https://www.ks.uiuc.edu/Research/vmd/current/ug.pdf

36. Kadau K, Germann TC, Lomdahl PS, Holian BL, Microscopic view of structural phase transitions induced by shock waves, Science 2002; 296:1681-1684. Available:https://pubmed.ncbi.nlm.nih.gov/12040192/

37. Ismail AE, Greathouse JA, Crozier PS, Foiles SM, Electron-ion coupling effects on simulations of radiation damage in pyrochlore waste forms, J. Phys. Condens. Mat. 2010;22(22):225405-225412. Available:https://pubmed.ncbi.nlm.nih.gov/21393744/

38. Vemparala S, Karki BB, Kalia RK, Nakano A, Vashishta P, Large-scale molecular dynamics simulations of alkanethiol self-assembled monolayers, J. Chem. Phys. 2004;121(9):4323–4330. Available:https://pubmed.ncbi.nlm.nih.gov/15332982/

39. Senjaya D, Supardi A, Zaidan A, Theoretical formulation of amorphous radial distribution function based on wavelet transformation, AIP Conference Proceedings, 2020;2314:020001. Available:https://aip.scitation.org/doi/abs/10.1063/5.0034410

40. Mansoori GA, Radial Distribution Functions and their Role in Modeling of Mixtures Behavior, Fluid Phase Equilibria 1993; 87:1–22.

Available:https://www.sciencedirect.com/science/article/abs/pii/037838129385015E

41. Xuelong W, Sha T, Qing YX, Enyuan H, Pair distribution function analysis: Fundamentals and application to battery materials, Chinese Physics B 2020; 29(2): 028802.
Available:https://iopscience.iop.org/article/10.1088/1674-1056/ab6656

42. Marahatta AB, Quantum−Mechanical Investigation of Chemical Energetics and Electronic Stabilities of Microhydrated Protons $[H^+(H_2O)_n]$, Int. J. Prog. Sci. Tech. 2020; 22(2): 290−303.
Available:https://ijpsat.org/index.php/ijpsat/article/view/2006

43. Feng C, Li Y, Qu K, Zhang Z, Mechanical behavior of a hydrated perfluorosulfonic acid membrane at meso and nano scales, RSC Advances 2019; 9(17): 9594-9603.
Available:https://pubs.rsc.org/en/content/articlelanding/2019/ra/c9ra00745h

44. Guccini V, Carlson A, Yu S, Lindbergh G, Lindström RW, Alvarez GS, Highly proton conductive membranes based on carboxylated cellulose nanofibres and their performance in proton exchange membrane fuel cells, J. Mater. Chem. A, 2019; **7**: 25032−25039.
Available:https://pubs.rsc.org/en/content/articlelanding/2019/ta/c9ta04898g

45. Vijayakumar M, Govind N, Li B, Wei X, Nie Z, Thevuthasan S, Sprenkle V, Wang W, Aqua-vanadyl ion interaction with Nafion® membranes, Front. Energy Res. 2015; 3(10):1-5.
Available:https://www.frontiersin.org/articles/10.3389/fenrg.2015.00010/full

46. Marahatta AB, Coordination Chemistry of Vanadium Aquo Complex Ions in Oxidation States +II, +III, +IV, and +V: A Hybrid-Functional DFT Study, Int. J. Prog. Sci. Tech. 2020; 24(1): 645-661.
Available:https://ijpsat.org/index.php/ijpsat/article/view/2496

47. Hinkle KR, Jameson CJ, Murad S, Transport of Vanadium and Oxovanadium Ions Across Zeolite Membranes: A Molecular Dynamics Study, J. Phys. Chem. C 2014;118(41): 23803-23810.
Available:https://pubs.acs.org/doi/abs/10.1021/jp507155s

Peer-review history:
The peer review history for this paper can be accessed here:
https://www.sdiarticle5.com/review-history/97168